Advanced Steel Construction – Vol. 19 No. 4 (2023) 329–340
DOI:10.18057/IJASC.2023.19.4.2

INVESTIGATING FATIGUE MECHANISMS AND CRACK GROWTH IN 20MNTIB STEEL HIGH-STRENGTH BOLTS: AN EXPERIMENTAL AND SIMULATION STUDY

Jin-Feng Jiao [1, 2], Li-Xuan Fan [2], Yong Liu [3], Hong-Gang Lei [2] and Qi Guo [2, *]

[1] *Department of Architecture, Lyuliang University, Lyuliang, Shanxi Province, China*
[2] *College of Civil Engineering, Taiyuan University of Technology, Taiyuan, Shanxi Province, China*
[3] *Shandong Electric Power Engineering Consulting Institute Corp., Ltd, Jinan, Shandong Province, China*
** (Corresponding author: E-mail: guoqi_tony@163.com)*

ABSTRACT

In this paper, axial-tensile, constant-amplitude fatigue experiments are performed on M24 high-strength bolts with grade 8.8 fabricated from 20MnTiB steel with a stress ratio (*R*) of 0.3, and their crack development is simulated. The stress range-fatigue life (*S–N*) curve is derived by using the experimental results. The fatigue mechanism is then investigated through strain and fractographic analyses. Moreover, the extended finite element method (XFEM) is applied for assessing the fatigue crack propagation behavior of the high-strength bolts. The findings reveal that the 20MnTiB steel bolt exhibits a threshold fatigue strength of 140.77 MPa at two million loading cycles, which is 1.68 times greater than the corresponding value for 35K steel bolts at the same stress ratio. The bolt's stable deformation stage constitutes 87% of its total fatigue life. The XFEM is capable of accurately predicting the fatigue crack propagation trajectory and the lifespan of the high-strength bolts. Our analysis indicates that the crack initially propagates predominantly along the bolt's circumferential direction, accounting for 85% of the overall crack propagation life, before transitioning to unstable growth and experiencing an exponential increase in length.

ARTICLE HISTORY

Received: 9 December 2022
Revised: 10 May 2023
Accepted: 11 May 2023

KEYWORDS

High-strength bolt;
Constant-amplitude fatigue;
Fatigue fracture propagation;
Extended finite element method (XFEM);
Stress intensity factor (SIF)

1. Introduction

High-strength bolts play a crucial role in securing prefabricated steel structures and are extensively employed in offshore wind turbines and grid structures [1-3]. Despite their resilience, bolts are exposed to cyclic loads throughout their service life. Although they may not fail instantly under such loading conditions, the progressive accumulation of fatigue damage ultimately compromises their mechanical properties, leading to engineering failures [4]. Consequently, the fatigue behavior of bolts warrants investigation.

Numerous studies have been conducted to explore the fatigue properties of high-strength bolts, including research by Yang et al. [3,5], Qiu et al. [6], Jiao et al. [7,8], Liu et al. [9], Tizani et al. [10], and Schaumann and Rasmus [11]. These works focused on factors influencing bolt fatigue properties, such as geometry, types, and surface heat treatment. Jiang et al. [12] introduced a method to calculate the critical loosening load of bolted connections under lateral loading. The wealth of fatigue test data obtained has enhanced the understanding of high-strength bolt fatigue properties. As a result, Bartsch and Feldmann [13] recommended adopting the fatigue classification in EC 3-1-9 after reviewing approximately 573 groups of experimental fatigue data on high-strength bolts with varying constructional details.

Furthermore, the fracture surface retains essential information about the bolt's fatigue process, recording a wealth of specific fatigue data. Consequently, fractography analysis can be employed to study the fatigue failure process [14]. Maljaars and Euler [15] and Lochan et al. [16] reported that bolts subjected to tensile force frequently fractured at the first engaged thread due to stress concentration caused by the thread shape. Kaushik and Anup [17] argued that fiber trajectories and microscopic fracture texture micro-flows could indicate the crack growth path. Liu et al. [18] also determined the fatigue crack growth rate through fractography analysis using scanning electron microscopy (SEM).

The advancement of finite element modeling has led to an increasing number of researchers adopting this technique to uncover the fatigue failure mechanisms of components. Wang et al. [19], for example, demonstrated that the drilling position significantly influenced the peak stress on the hole edge using finite element analysis. Fang et al. [20] simulated crack propagation direction and path in a perforated plate using Abaqus, with results closely aligning with experimental data. In another study, Gu et al. [21] calculated the stress intensity factor (SIF) of cold-formed, circular, hollow-section (CFCHS), T-type, welded joints using Ansys software and developed a method for assessing the fatigue life of such joints. The extended finite element method (XFEM) is the most prevalent technique for investigating fatigue crack propagation issues. Researchers such as Shi et al. [22], Malekan et al. [23], and Shu et al. [24] found that XFEM could accurately predict fracture location, crack propagation path, fatigue fracture morphology, and fatigue life of standard specimens. Additionally, Samai et al. [25], Bergara et al. [26], and Ngoula et al. [27] employed XFEM to examine fatigue crack growth in connection plates with varying joints, aero-engine blades, and cruciform welded joints, respectively. Pandey et al. [28] simulated the fatigue life of compact tension (CT) specimens and turbine disks composed of different materials using continuum damage mechanics and XFEM. Lin and Smith [29] predicted the fatigue crack propagation life of cracked slabs, while Yang and Kuang [30] and Kumar and Prakash [31] analyzed the effects of thread angle, mesh size, and crack size on the SIF of bolts using XFEM. These analyses achieved satisfactory prediction accuracy.

In summary, previous research has conducted numerous experiments on factors affecting the fatigue properties of bolts. Furthermore, the material composition of a bolt significantly influences its fatigue behavior [32]. Consequently, stress range–fatigue life (S–N) data derived from tests on bolts made of different materials can offer valuable insights for accurately predicting their fatigue life. However, the study of fatigue crack propagation in high-strength bolts remains limited.

This paper examines the constant-amplitude fatigue properties of 20MnTiB steel high-strength bolts at a stress ratio (R) of 0.3. An S–N curve is constructed based on the test data. The results are then compared with existing research data on the fatigue properties of 35K steel high-strength bolts to determine the impact of material properties on bolt fatigue behavior. The fatigue fracture process and characteristics of the fatigue-fractured surfaces are analyzed using strain analysis and fractographic analysis. Furthermore, the crack propagation process of the bolts is modeled using XFEM, and the SIF at the crack front and the crack characteristics at different propagation stages are discussed. Finally, the crack propagation law and fracture mechanism of high-strength bolts are investigated.

2. Experimental

2.1. Preparation of specimens

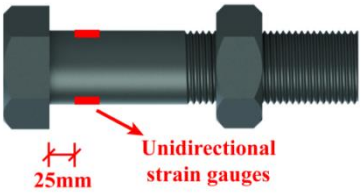

Fig. 1 Specimen design

The fatigue test was carried out on grade 8.8 M24 high-strength bolts made from 20MnTiB steel, a material frequently used in engineering applications. The rod was ground 25 mm away from the bolt head to attach a strain gauge, which monitored changes in the bolt rod's strain during the test and ensured the correct application of tightening torque, as depicted in Fig. 1.

2.2. Fundamental mechanical properties

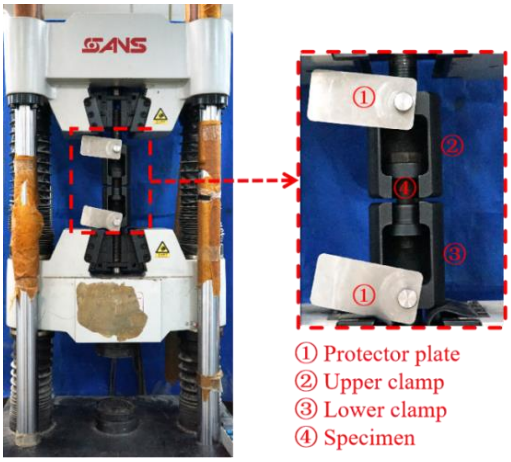

Fig. 2 Electrohydraulic servo universal testing machine

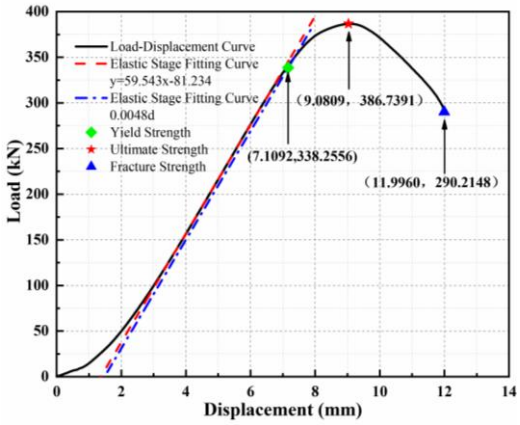

Fig. 3 Load–displacement curve

The static test was employed for determining the bolts' mechanical properties, design a suitable loading system for the fatigue experiments, and provide a constitutive relationship for subsequent finite element analysis. In accordance with ISO 898-1:2013 standard [33], three specimens were randomly chosen for testing. An electrohydraulic servo universal testing machine performed the tensile test using force control (Fig. 2), with a loading rate of 2.7 kN/s.

The test data were processed, and load–displacement curves were generated. Fig. 3 illustrates the load–displacement curve for one specimen. Elastic modulus (E), yield strength (f_y), and ultimate strength (f_u) were calculated for the three specimens after fracture, and the average values were taken, as presented in Table 1.

Table 1
Mechanical attributes of the high-strength bolt

Test results	Mechanical properties		
	E (MPa)	f_y (MPa)	f_u (MPa)
20MnTiB	2.66×10^5	780.30	861.80

2.3. Constant-amplitude fatigue testing

Considering the three structural classifications of bolts in relevant specifications [34,35,36,37], the fatigue strength of the base metals in bolted end-plate connections is the highest for 2 million loading cycles, followed by the shear fatigue of the bolt. The tensile fatigue strength of the bolt is the lowest, with a difference of over 50% compared to the other two. This suggests that bolt fatigue under tension is disadvantageous, and this section investigates the constant-amplitude fatigue properties of high-strength bolts subjected to axial tension.

2.3.1. Fatigue testing system

Given the experimental conditions and referring to the standard static tensile testing device [33] and previous related studies [7,8], a simplified loading device for axial–tensile fatigue experiments was designed and installed in the MTS testing machine (Figs. 4a and 4b).

To ensure sufficient stiffness and stability, the thickness of the clamp base plate was set at 25 mm, and stiffening ribs were welded to both sides of the device. Additionally, the loading device was aligned so that the bolt only experienced axially tensile loads during testing. A torque wrench pretensioned the bolt while monitoring the strain to guarantee proper pretensioning application (Fig. 4c).

The fatigue test began after completing the above procedures. Throughout the test, the strain changes on the bolt were recorded every 30 minutes to estimate crack growth. The fatigue test concluded when the bolt failed.

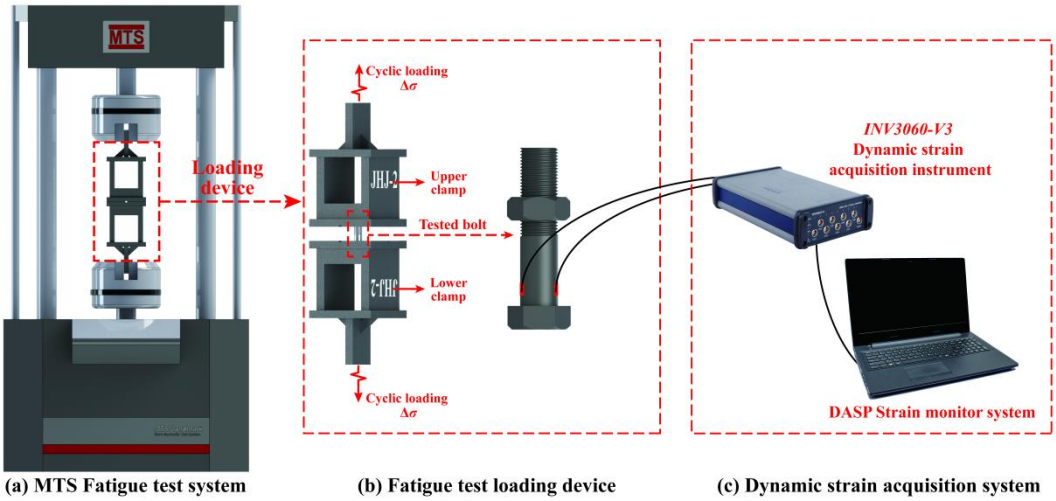

Fig. 4 Fatigue testing setup

2.3.2. Loading scheme

The stress level in the fatigue test primarily consists of two numerical indicators: minimum stress (σ_{min}) and maximum stress (σ_{max}). With a fixed stress ratio (R), the stress level can be represented by the stress range ($\Delta\sigma$). The stress level of the loading scheme corresponding to the bolt was calculated based on its effective cross-sectional area.

The present research explored the fatigue characteristics of high-strength bolts at an R value of 0.3. A sinusoidal wave with a frequency of 7 Hz was

employed to apply the fatigue load. The stress range ($\Delta\sigma$) varied from 180 to 280 MPa in order to investigate the bolts' fatigue behavior under elevated stress levels. Prior to the fatigue test, a pretensioning torque (T) given by Eq. (3) was applied to the bolt to simulate its actual stress state.

$$R = \sigma_{min}/\sigma_{max} \quad (1)$$

$$\Delta\sigma = \sigma_{max} - \sigma_{min} \quad (2)$$

$$T = K \cdot F \cdot d_0 \quad (3)$$

where K represents the tightening torque coefficient related to surface treatment, F denotes the pretensioning force, and d_0 represents the high-strength bolt's nominal diameter, which equals 24 mm. Table 2 displays the loading scheme for this test.

Table 2
The loading scheme and fatigue test results of the bolt with an R of 0.3

Specimen	σ_{max}, (MPa)	σ_{min}, (MPa)	$\Delta\sigma$, (MPa)	T, (N·m)	Fatigue life, N, ($\times 10^4$)
S-01	257.14	77.14	180	330	163.83
S-02	271.43	81.43	190	440	134.41
S-03	285.71	85.71	200	350	90.64
S-04	300.00	90.00	210	270	83.97
S-05	314.29	94.29	220	370	55.29
S-06	328.57	98.57	230	270	38.47
S-07	342.86	102.86	240	370	45.72
S-08	357.14	107.14	250	370	17.37

3. Results

All bolts underwent fatigue fractures, with their fatigue lives presented in Table 2.

3.1. S–N curves

Fig. 5 illustrates the double logarithmic regression analysis relating stress range ($\Delta\sigma$) to fatigue loading cycles (N). All test results are uniformly distributed near the fitting line, with a 95% confidence level. A negative correlation exists between $\Delta\sigma$ and N.

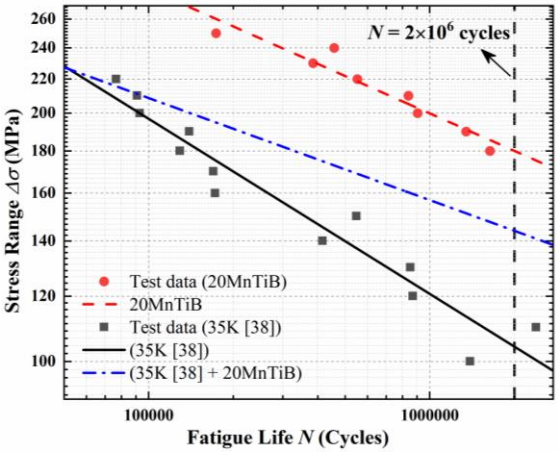

Fig. 5 The double logarithmic regression curve of the stress range versus the fatigue loading cycles

The S–N curve for the 35K steel high-strength bolt [38] is also displayed at the same R value. Additionally, Fig. 5 includes another curve that fits data for both 35K [38] and 20MnTiB steel bolts, enabling a comparison of the fatigue properties between M24 high-strength bolts made from 20MnTiB and 35K steel. The fatigue characteristics of the 35K steel bolt are less favorable compared to those of the 20MnTiB steel bolt at the same stress range, indicating that material properties have an impact on the bolt's fatigue life.

Table 3 shows the fatigue properties of bolts made of 20MnTiB and 35K steel. Both curves modeling the 20MnTiB and 35K steel [38] bolts exhibit a relatively high goodness of fit. When the number of loading cycles reaches 2×10^6, the fatigue strength of the 20MnTiB steel bolt is 1.68 times greater than that of the 35K steel bolt. This is because fatigue properties are associated with the yield strength to ultimate strength ratio of the material: a higher ratio facilitates stress redistribution of the material at the notch or thread root [39]. The yield strength to ultimate strength ratio of the 20MnTiB and 35K steel bolts is 0.91 and 0.75 [38], respectively, with the former being 1.21 times higher than the latter, resulting in superior fatigue properties for the 20MnTiB steel bolt.

Moreover, the fatigue strength at 2×10^6 loading cycles to yield strength ratio, obtained from the static test for the 20MnTiB and 35K steel bolts, is only 0.18 and 0.14, respectively. This indicates that high-strength bolts may experience fatigue fractures under cyclic stress levels significantly below their yield strength [16], warranting attention.

Nonetheless, the correlation coefficient of the S–N curve obtained by fitting the test data on the 35K [38] and 20MnTiB steel bolts together decreases to 0.251, rendering this curve unrepresentative. This suggests that material properties considerably impact fatigue life. Thus, incorporating a correction factor into the S–N curve assists in obtaining the actual fatigue strength of the bolts, serving as a reference for engineering design practice.

Table 3
S–N curve and fatigue strength comparison for high-strength bolts fabricated from distinct materials

Test data	S–N curves	Correlation coefficient (R^2)	$[\Delta\sigma]_{2\times10^6}$	$[\Delta\sigma]_{2\times10^6}/f_u$
20MnTiB steel	$\lg(\Delta\sigma) = -0.151 \cdot \lg N + 3.205 \pm 0.107$	0.918	140.77 MPa	0.18
35K steel [38]	$\lg(\Delta\sigma) = -0.212 \cdot \lg N + 3.356 \pm 0.095$	0.933	83.83 MPa	0.14
35K steel [38] + 20MnTiB steel	$\lg(\Delta\sigma) = -0.124 \cdot \lg N + 2.938 \pm 0.276$	0.251	76.36 MPa	—

3.2. Analysis of dynamic strain

The strain data are closely associated with the local shape of the component and can depict the stress redistribution near the sensor. The local component damage is intuitively characterized, and the curve trend can qualitatively assess the crack growth process. The strain data gathered on the bolt rod are illustrated in Fig. 6, with the points representing the average strain amplitude at each time.

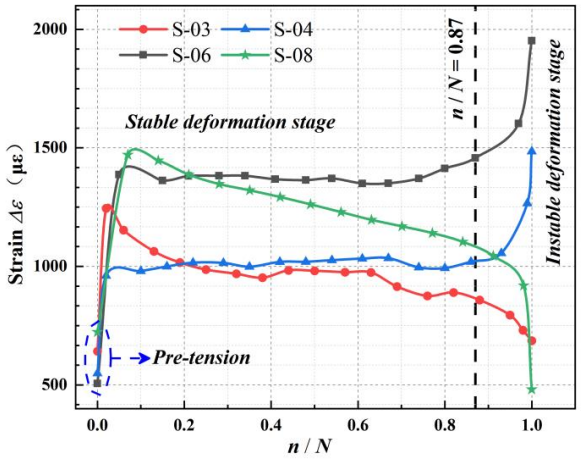

Fig. 6 The association between strain and fatigue loading cycles of the test specimens

Fig. 6 reveals that the deformation of the bolt can be categorized into stable and unstable phases. The strain does not increase from zero due to the application of the pretensioning force before the fatigue test. After the fatigue load is applied, the mean strain amplitude experiences significant changes. Subsequently, as the test progresses, the average strain remains nearly constant, and the fatigue crack expands consistently during this period. This phase constitutes the primary part (i.e., 87%) of the fatigue life and is the stable propagation life of fatigue cracks. The subsequent phase is the variable deformation stage. Due to the sufficient accumulation of fatigue damage in the previous stage, the bolt undergoes rapid deformation, and the fatigue crack grows inconsistently; thus, fracture occurs swiftly. The crack origin location can be inferred from the strain variation, that is, the crack begins near the gauge with the strain gradually decreasing. This is because the crack initiation and opening contribute to the eccentricity of the initial axial tension and the reduction of the load on the crack side, subsequently decreasing the average strain. Conversely, the strain of the opposite gauge exhibits a rising trend due to the increase in the eccentric load.

3.3. Fractographic examination

Fractographic analysis is an essential method to investigate the fatigue fracture of components. This section inspects the macroscopic fracture morphology characteristics of the high-strength bolts and then analyzes their microscopic fracture morphology and roughness of the fracture surface using SEM and 3-D morphology scanning, as displayed in Figs. 7 and 8, to deduce their fracture mechanisms at different stress levels.

3.3.1. Macroscopic fracture

Fig.9 shows that all specimen fractures occur at the root of the first or second engaged thread of the bolt. This is due to the significant stress concentration caused by the cross-sectional variation at the bolt thread.

Fig. 7 The scanning electron microscope

Fig. 8 The Keyence VK-X1000 3D noncontact morphology scanner

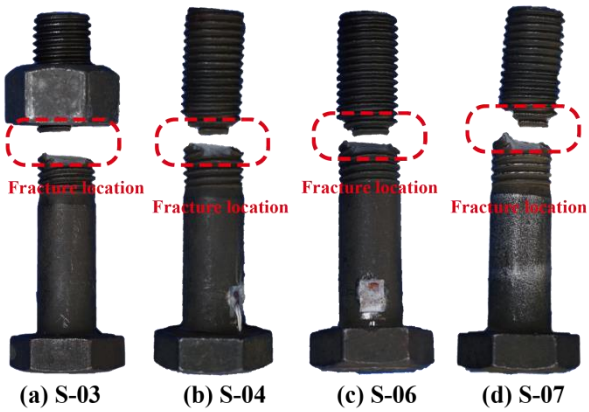

Fig. 9 The failure fracture position of the high-strength bolts

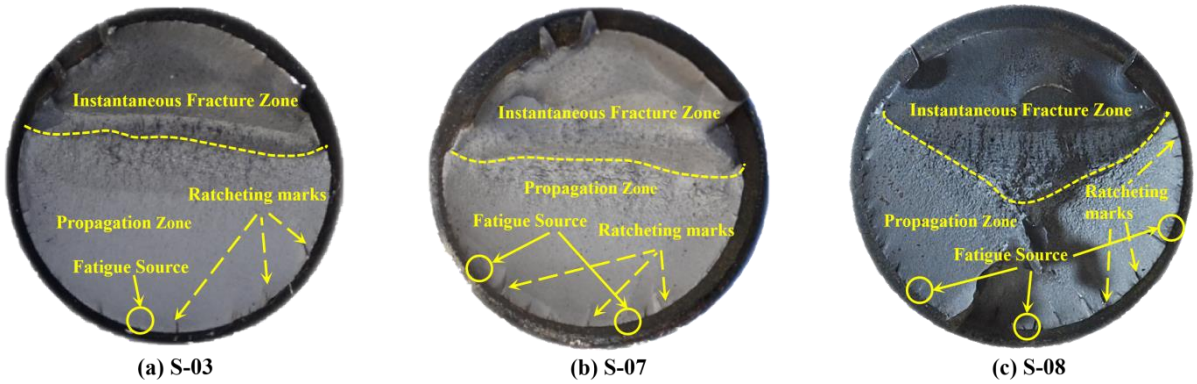

Fig. 10 Macroscopic fracture morphology of the high-strength bolts

Fig. 10 displays three representative specimens, specifically S-03, S-07, and S-08, taken as examples to show the detailed fatigue fracture features. The fracture can be categorized into three areas: the fatigue origin, the crack growth zone, and the instantaneous fracture zone. It is observed that all fatigue origins form on the surface of the specimens, and the fatigue fractures display features of multiple crack initiation, as indicated by the ratcheting marks. These marks

result from the nucleation and connection of multiple cracks at different points, forming steps on the fracture surface. The steps extending from the origin zone grow more significantly in the growth zone, and noticeable radial streaks form. The crack growth zone occupies most of the fracture area, which is rougher and darker than the previous zone. The sudden fracture area exhibits the roughest texture, and a noticeable shear lip can be observed. Because the bolt is notched, the stress concentration on the outer surface is significant, and the crack growth rate on both sides is higher than that in the middle; thus, the crack front is a convex arc.

Upon examining the macroscopic fracture morphology of the cross sections of the high-strength bolts, it becomes evident that an elevated stress level can augment the quantity of ratcheting marks on the fracture surface. This suggests the potential presence of multiple crack sources on the fracture surface, resulting in a complex fracture morphology. The quantitative analysis of the fractures across all specimens demonstrates that the crack growth portion constitutes 55%-75% of the total surface area (A), signifying that it forms the primary fatigue life. This portion exhibits a negative relationship with the stress level. In particular, a higher stress level hastens the crack propagation rate, meaning that fewer fatigue loading cycles are needed for the same length of crack propagation; thus, the area of the propagation zone diminishes, as depicted in Fig. 11.

Additionally, the swift expansion of the crack leads to a rapid decline in the effective cross-sectional area of the load-bearing capacity, causing the bolt to be incapable of withstanding high stress. Consequently, the bolt fails more rapidly, resulting in pronounced tear marks and a highly irregular surface in the instantaneous fracture zone.

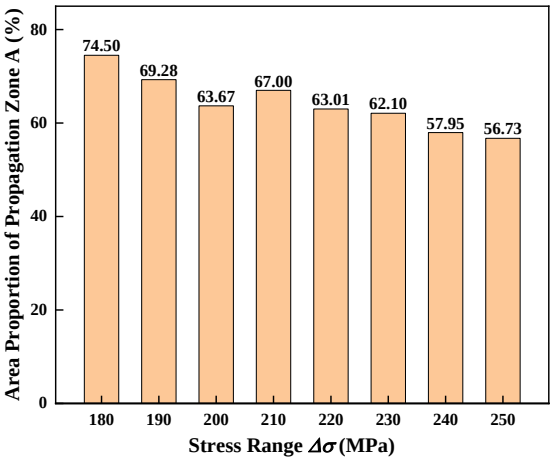

Fig. 11 The bar graph of the area proportion of the propagation zone versus the stress range

3.3.2. Microscopic fracture

Figs. 12–14 display the two-dimensional representations of the microscopic fracture morphology of the characteristic high-strength bolts subjected to high-cycle fatigue loading.

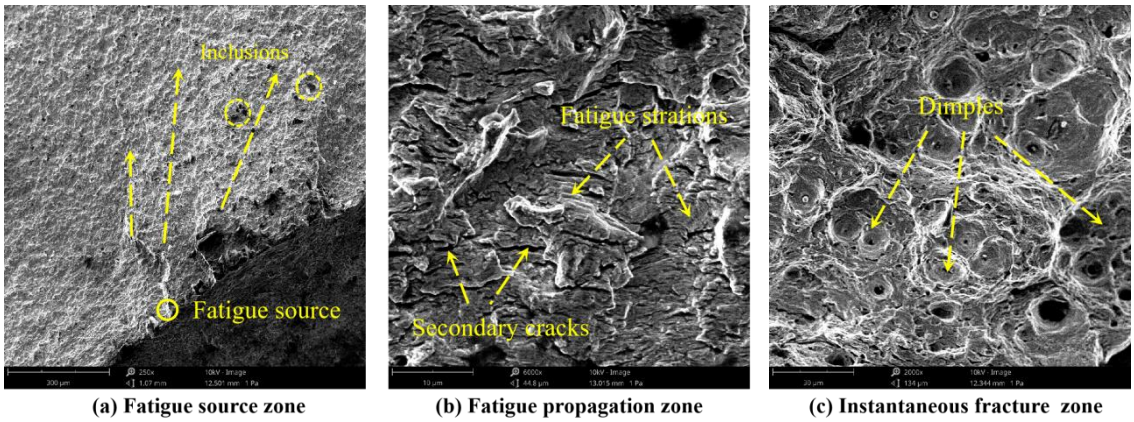

Fig. 12 Microscopic fracture analysis of specimen S-03

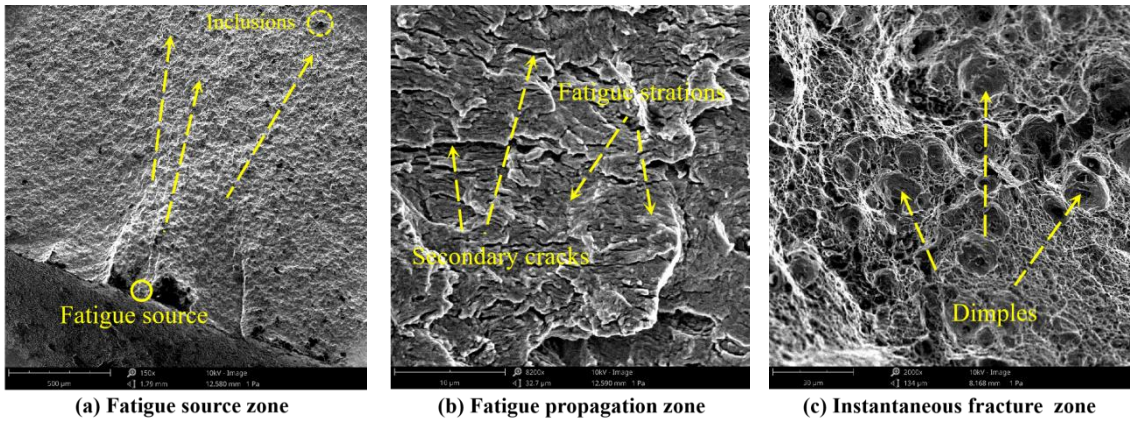

Fig. 13 Microscopic fracture analysis of specimen S-07

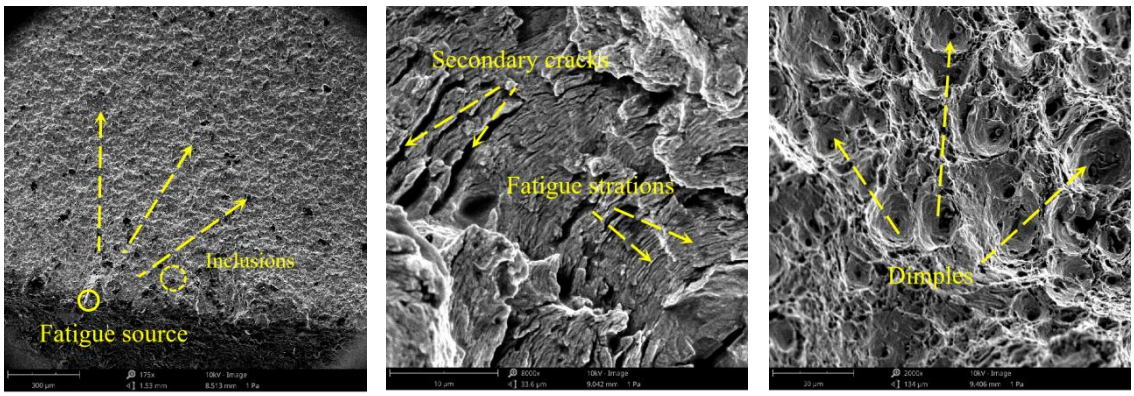

Fig. 14 Microscopic fracture analysis of specimen S-08

Cracks initiate in the fatigue source and develop further, with numerous radial rays present on the fracture surface. In this region, black specks are visible, which represent inclusions during fabrication, contributing to a reduction in the cross-sectional area's strength, as illustrated in Figs. 12(a), 13(a), and 14(a). The images also reveal that an increase in stress level results in more pronounced ratcheting marks and a higher density of radial rays, primarily due to heightened stress concentration at the bolt thread.

The conspicuous bright fatigue striation is a distinguishing feature in the fatigue propagation zone. This striation consists of a series of nearly parallel stripes with minor band bending in a wave-like pattern, perpendicular to the local crack propagation direction. Additionally, secondary cracks can be observed in this area, running parallel to the fatigue striations. These cracks exhibit a discontinuous distribution and a depth notably greater than that of the fatigue striations.

A comparison of Fig. 12(b), Fig. 13(b), and Fig. 14(b) indicates that a higher stress level results in larger spacing between fatigue striations. This suggests that elevated stress levels promote damage accumulation at the crack tip and an increased crack propagation rate; in other words, crack propagation values rise for the same loading cycles, and fatigue striation spacing expands. Consequently, this area displays a reduced reflective capacity, yielding a darker color. Moreover, the quantity and size of secondary cracks increase, correlating with the stress state at the crack front: a higher stress level corresponds to a more pronounced stress concentration.

The surface in the instantaneous fracture zone is the most uneven and coarse among the three regions. Some dimples, whose diameter and depth depend on the material properties and loading scheme, can be observed in this area. These dimples are either elliptical or circular, suggesting they form under tension. Their formation mechanism involves microscopic cavities within metals undergoing nucleation, growth, and accumulation until a plastic fracture occurs due to an axial load perpendicular to the fracture plane.

A comparison of Fig. 12(c), Fig. 13(c), and Fig. 14(c) reveals that dimples exhibit larger diameters and greater depths at higher stress levels, as increased stress accelerates pore nucleation and growth.

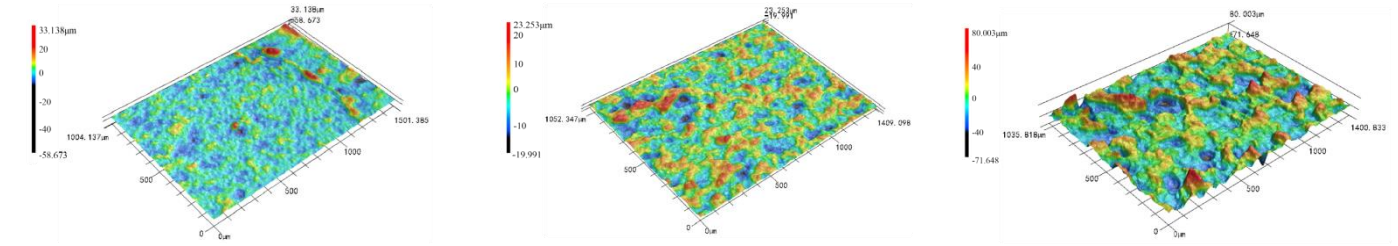

Fig. 15 3-D surface morphology of specimen S-03

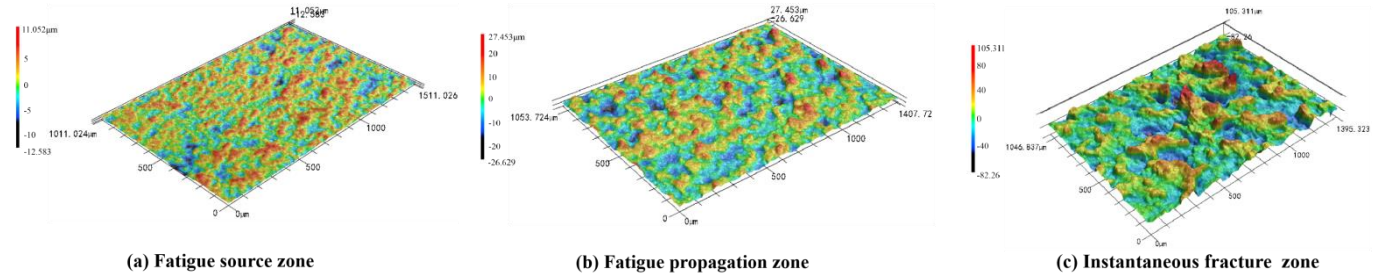

Fig. 16 3-D surface morphology of specimen S-07

Figs. 15 and 16 present two representative specimens, S-03 and S-07, as examples to illustrate the roughness of various zones. They indicate that as the crack propagates, the surface's concave and convex features intensify. It is apparent that the fracture surface is relatively smooth in the fatigue source zone, while a "topographic relief" characteristic emerges in the propagation zone. In the instantaneous fracture zone, the surface morphology exhibits greater fluctuations, interspersed with "ditches" and "gullies."

Fig. 17 demonstrates that the roughness at an identical position on the fracture surface is directly proportional to the stress level, as higher stress levels facilitate crack nucleation, resulting in a greater number of cracks and more convoluted and intricate crack propagation paths. Consequently, the fracture surface becomes rougher.

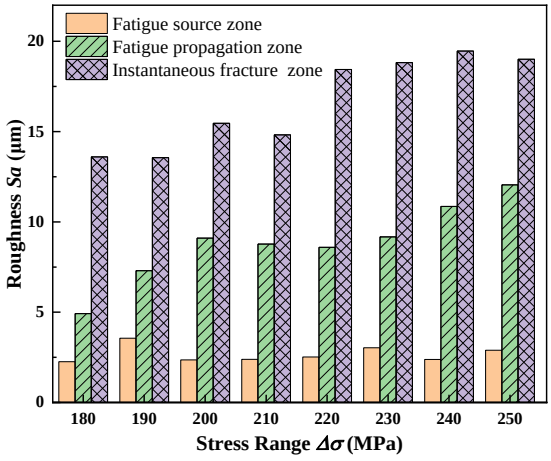

Fig. 17 Variation in roughness of different zones with the stress range

4. Finite element modeling of fatigue crack propagation in high-strength bolt

A finite element model is established employing the XFEM introduced by Abaqus software to examine the fatigue crack growth process of the 20MnTiB steel high-strength bolts. According to the test results and the existing research, the critical parameters are determined: the initial position of the crack, the crack shape, the initial size of the crack, the crack growth criterion, the material constant, the crack growth increment, and the cycle termination conditions. Then, the SIF at the bolt crack front is calculated. The fatigue crack growth process and fatigue life of the high-strength bolt are also predicted based on fracture mechanics. These findings can promote research on the fatigue crack propagation law and fracture mechanism of high-strength bolts.

4.1. XFEM validation

To confirm the accuracy of XFEM in calculating the SIF, a rectangular block with a crack is used as an example for calculating the stress intensity factor at the crack front. The dimensions of the rectangular block model are assigned: height, width, thickness, and crack length of 200, 100, 10, and 25 mm, respectively. A tensile stress (σ) of 25 MPa is applied to the model's upper and lower ends. The model's element type is C3D8R, with a global size of approximately 3.0 mm. The mesh size influences the SIF calculation accuracy; hence, the mesh size at the crack front is refined locally to examine its effect on the SIF, with refinement mesh sizes ranging from 0.1 to 1.2 mm. Fig. 18 illustrates the impacts of the mesh size in the refinement area and the integral path on the SIF simulation outcomes. Decreasing the mesh size improves the simulation results' accuracy. Additionally, the SIF exhibits significant fluctuations with a small integral path but stabilizes from the sixth integral path onwards, in line with the theory that the integral value is path-independent, as demonstrated in Fig. 18. Consequently, the average value of the SIF on the 7th, 9th, and 10th paths is used for subsequent analyses.

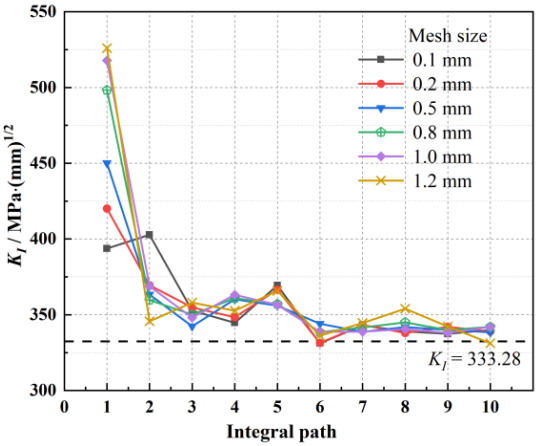

Fig. 18 Variation in stress intensity factor with integral path at different mesh sizes

The theoretical expression of the SIF for this example is derived as follows [40]:

$$K_I = F\left(\frac{a}{b}\right)\sigma\sqrt{\pi a} \tag{4}$$

where $F\left(\frac{b}{a}\right) = \frac{1+2\left(\frac{b}{a}\right)}{1-\left(\frac{a}{b}\right)^{3/2}}\left[\begin{array}{l}1.1200-3.6822\left(\frac{b}{a}\right)+11.9543\left(\frac{b}{a}\right)^2-25.8521\left(\frac{b}{a}\right)^3 \\ +33.0976\left(\frac{b}{a}\right)^4-22.4422\left(\frac{b}{a}\right)^5+6.1783\left(\frac{b}{a}\right)^6\end{array}\right]$, and K_I is calculated at 332.46 MPa·mm$^{1/2}$ using Eq. (4).

Table 4 compares the XFEM results with the theoretical calculations.

Table 4
The calculation results of the SIF under different mesh sizes.

XFEM	Mesh size (mm)						Theoretical calculations of SIF, K_I, (MPa·mm$^{1/2}$)
	0.1	0.2	0.5	0.8	1.0	1.2	
K_I (MPa·mm$^{1/2}$)	338.80	339.67	340.10	340.27	340.17	342.47	333.28
Difference (%)	1.66%	1.92%	2.05%	2.10%	2.17%	2.70%	

The difference between SIF values calculated using XFEM and the theoretical method is within 3.00%, validating the accuracy of K(I) determined by XFEM. Considering the model's computational accuracy and efficiency, the mesh size of the refinement region is set at 0.5 mm for subsequent analyses.

4.2. Extended finite element model of high-strength bolt

The bolt thread angle has a negligible effect on stress concentration and the SIF when less than 4° [31]. Thus, to enhance calculation efficiency, the thread angle for the bolt is disregarded, as depicted in Fig. 19.

The material properties introduced into the model include yield strength and ultimate strength of 780.30 and 861.80 MPa, respectively. Young's modulus and Poisson's ratio of the model are set at 2.66 × 10^5 MPa and 0.3, respectively.

Two analysis steps, 1 and 2, are established to calculate the $K_{I,\min}$ and $K_{I,\max}$ of the bolt under minimum and maximum loads, respectively.

Fig. 19 presents the loading and boundary conditions of the model. Two reference points, RP-1 and RP-2, are positioned on the upper and lower surfaces of the model, respectively, and are coupled with the two surfaces. The axial load is applied to the model at point RP-1, while a fixed boundary condition (UX = UY = UZ = URX = URY = URZ = 0) is assigned at point RP-2. Table 5 displays the model's loading scheme.

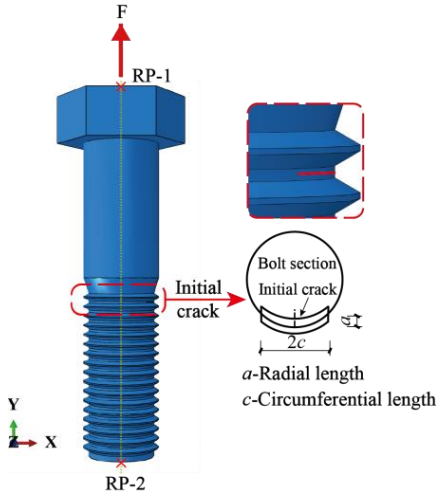

Fig. 19 Bolt model with a surface crack in the thread root region

Table 5
Loading scheme for simulating the fatigue crack propagation process

Model	F, (kN)		σ, (MPa)		$\Delta\sigma$, (MPa)	T, (N·m)	R
	F_{max}	F_{min}	σ_{max}	σ_{min}			
M-1	80.69	21.21	228.57	65.57	160		
M-2	85.73	25.72	242.86	72.86	170	360	0.3
M-3	90.77	27.23	257.14	77.14	180		

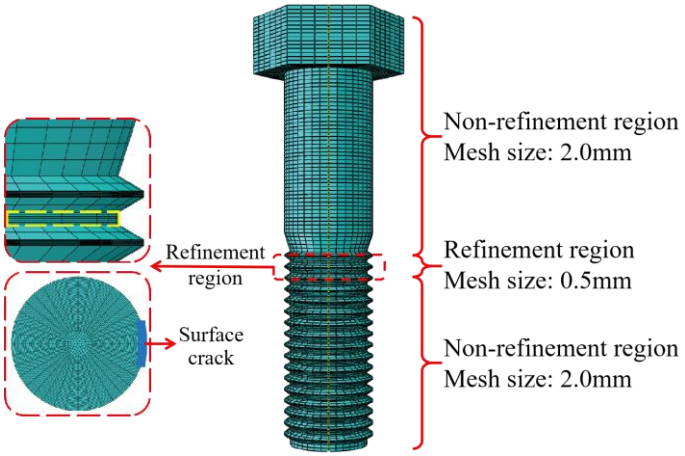

Fig. 20 The meshed model of the bolt

The model's element type is C3D8R, with a global size of approximately 2.0 mm. The first two threads' mesh is refined to a size of 0.5 mm, as shown in Fig. 20.

Fatigue test results and prior studies [8,15,16,26] indicate that fatigue cracks are prone to appear at the root of the first or second meshed thread of the high-strength bolt, so a sharp initial crack is introduced. The crack front shape is assumed to be a fan ring based on fractographic analysis and model convergence, as depicted in Fig. 19.

4.3. Fatigue crack propagation modeling

4.3.1. Crack propagation criteria and material parameters

Fracture mechanics is utilized to investigate crack propagation in this section. The Paris formula [41] is the most widely used crack growth criterion, reflecting the crack growth rate in different stages by selecting appropriate material constants.

$$\frac{da}{dN} = C(\Delta K_I^a)^m \tag{5}$$

$$\frac{da}{dN} = C(\Delta K_I^c)^m \tag{6}$$

where a and c represent the circumferential and radial length of the crack, respectively, N denotes the number of loading cycles, C and m are material constants, $\Delta K_I^a = K_{I,\max}^a - K_{I,\min}^a$, and $\Delta K_I^c = K_{I,\max}^c - K_{I,\min}^c$. The values of C and m, the threshold value (ΔK_{th}), and the fracture toughness (K_{Ic}) in different propagation stages are determined by the recommended values of Eurocode [43], as listed in Table 6.

Table 6
Recommended material constants for fatigue crack growth [45].

R	Stage I		Stage II		Threshold value, ΔK_{th}, (MPa·(mm)$^{1/2}$)	Boundary of stage I and stage II, ΔK_I, (MPa·(mm)$^{1/2}$)	Fracture toughness, K_{IC}, (MPa·(mm)$^{1/2}$)
	C	m	C	m			
0.3	1.21×10^{-26}	8.16	3.98×10^{-13}	2.88	127.20	363.00	3475.00

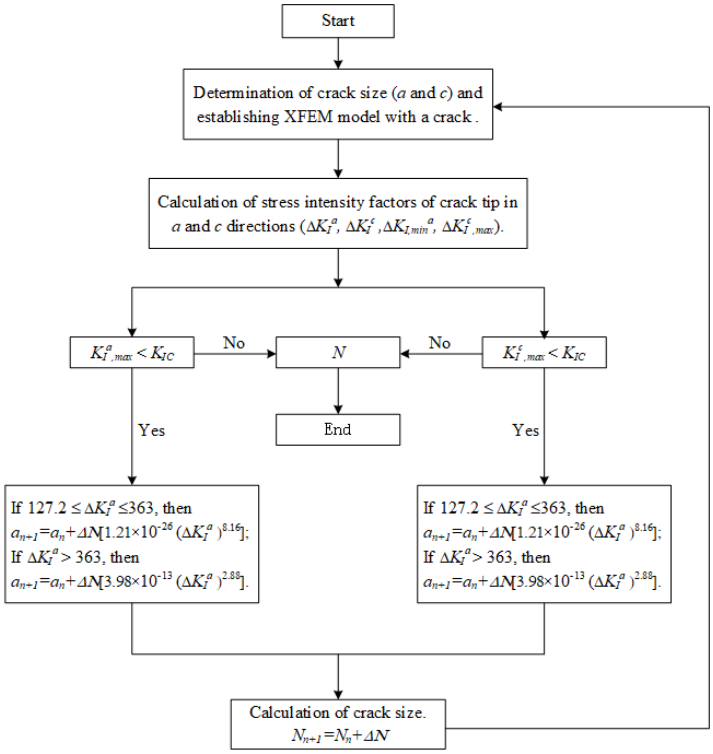

Fig. 21 Flow chart for iterative simulation of the fatigue crack propagation process [44]

4.3.2. Modeling process

Hirt and Fisher [43] inferred that a circle with a radius of 1.016 mm could represent the initial crack size, and the precision of the magnetic particle flaw detection method, typically used for detecting surface cracks, was approximately 1 mm. Consequently, the initial crack's circumferential length (twice c) is set at 1 mm, and the radial length (a) is assumed to be 0.5 mm. Next, a suitable increment of loading cycles (ΔN) is selected to ensure that the increase in a or c is more than one mesh size (0.5 mm). The fatigue life is predicted by calculating a and c incrementally until the cycle termination conditions are met.

Fig. 21 displays the flow chart for the iterative simulation of the fatigue crack propagation process. The crack is presumed not to propagate when $\Delta K_I \leq$ 127.2 MPa·(mm)$^{1/2}$.

4.3.3. Modeling results

Tables 7–9 present the iterative results of crack propagation at different stress ranges.

Table 7
Iterative calculation results of crack propagation at $\Delta\sigma$ of 160 MPa

Crack size (mm)		Fatigue life, N, ($\times 10^4$)	ΔK_I (MPa·(mm)$^{1/2}$)		K_{max} (MPa·(mm)$^{1/2}$)	
a	c		ΔK_I^a	ΔK_I^c	$K_{I,\max}^a$	$K_{I,\max}^c$
0.5	0.5	0	261.40	399.70	621.03	945.10
0.5	1.1	5	118.57	406.30	243.75	736.67
0.5	1.8	10	203.14	305.80	482.08	705.58
0.6	2.3	30	318.80	368.24	695.96	909.14
0.8	2.8	35	376.44	368.28	830.54	823.44
1.3	3.3	40	403.13	373.04	863.03	832.38
1.9	3.8	45	519.48	431.25	1010.86	1003.96
3.2	4.6	50	874.12	477.06	1789.24	1542.95
5.6	5.0	52	1717.53	1324.81	3316.30	3049.33
6.4	5.4	52.1 (Fatigue failure)	3430.28	2229.06	5652.93	3578.97

Table 8
Iterative calculation results of crack propagation at $\Delta\sigma$ of 170 MPa

Crack size (mm)		Fatigue life, N, ($\times 10^4$)	ΔK_I (MPa·(mm)$^{1/2}$)		K_{max} (MPa·(mm)$^{1/2}$)	
a	c		ΔK_I^a	ΔK_I^c	$K_{I,\max}^a$	$K_{I,\max}^c$
0.5	0.5	0	278.10	428.17	651.50	994.47
0.6	1.3	5	106.17	533.35	272.95	750.18
0.6	2.7	10	264.23	343.33	626.08	789.38
0.6	3.3	20	325.42	371.18	620.03	840.78
0.8	3.8	25	328.60	471.63	715.38	982.81
1.0	4.8	30	483.71	442.56	943.38	876.05
2.1	5.6	35	822.81	836.05	1335.17	1622.20
3.1	6.6	36	1081.52	1181.66	1891.62	2102.88
3.7	7.5	36.3	1384.26	1493.86	3008.30	3293.34
4.1	7.7	37 (Fatigue failure)	2860.44	2770.41	4951.78	4533.09

Table 9
Iterative calculation results of crack propagation at $\Delta\sigma$ of 180 MPa

Crack size (mm)		Fatigue life, N, ($\times 10^4$)	ΔK_I (MPa·(mm)$^{1/2}$)		K_{max} (MPa·(mm)$^{1/2}$)	
a	c		ΔK_I^a	ΔK_I^c	$K_{I,\max}^a$	$K_{I,\max}^c$
0.5	0.5	0	296.58	461.17	676.82	1037.87
0.6	1.4	5	155.88	415.60	299.20	837.07
0.6	2.1	10	318.01	315.43	711.09	676.92
1.2	2.7	30	547.68	693.04	1240.72	1322.35
1.8	3.9	32	605.46	550.21	1148.93	1126.80
3.1	4.9	35	1264.46	1135.10	2147.14	1979.31
4.4	5.9	35.4	1792.18	717.53	3269.36	3149.89
5.4	5.9	35.5 (Fatigue failure)	2938.93	4182.75	4523.64	6580.71

Table 10
Comparison of simulated fatigue life of high-strength bolts with values fitted by the *S–N* curves at various stress ranges

Model	Stress range, $\Delta\sigma$, (MPa)	Fatigue life, N, (× 10^4)		N_s/N_f
		Simulated values, N_s	Values fitted by the *S–N* curves, N_f	
M-1	160	52.00	59.19	0.88
M-2	170	36.30	57.62	0.63
M-3	180	35.40	56.19	0.63
	Average value			0.71

Table 10 compares the simulated fatigue life of high-strength bolts with values determined by the S–N curves. The simulated fatigue life is 0.88, 0.63, and 0.63 times the fitted value at stress ranges of 160, 170, and 180 MPa, respectively, yielding an average value of 0.71, which is acceptable. These findings suggest that the numerical simulation of fatigue crack propagation devised in this study can accurately predict the fatigue life of high-strength bolts. Additionally, the differences can be attributed to the simulation results disregarding the crack initiation life, that is, the fatigue life from microscopic defects to macroscopically detectable cracks. Furthermore, the parameters employed in the crack propagation simulation are based on the conservative recommended values of Eurocode, ensuring sufficient safety.

5. Discussion

Fig. 22 illustrates the changes in crack length in both circumferential and radial directions concerning the loading cycles at different stress ranges during fatigue failure.

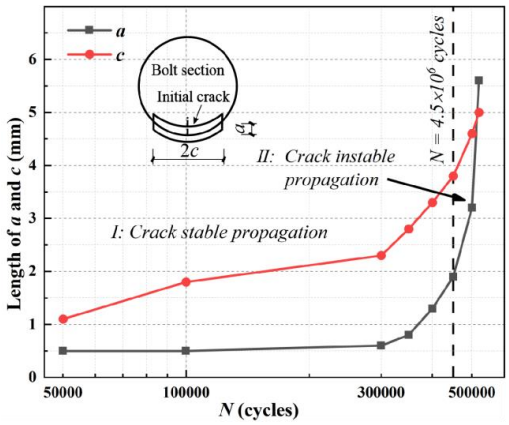

(a) $\Delta\sigma$ = 160 MPa

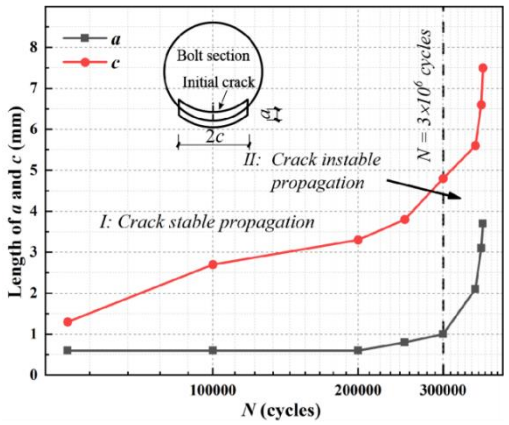

(b) $\Delta\sigma$ = 170 MPa

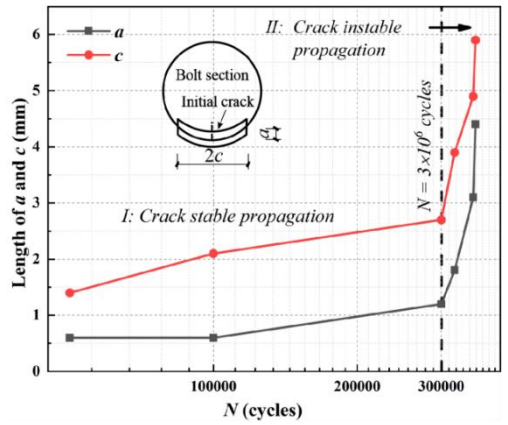

(c) $\Delta\sigma$ = 180 MPa

Fig. 22 The association between crack length and oading cycles at various stress ranges

Two distinct crack propagation phases are identified in the curves based on the crack length alteration: stable phase (I) and unstable phase (II). In phase I, the crack mainly expands slowly in the circumferential direction and exhibits a reduced growth rate in the radial direction. This phase encompasses 85% of the crack propagation life, which aligns well with the $\Delta\varepsilon$–n/N curve analysis outcomes from the tests, thus validating the feasibility of using XFEM for simulating crack propagation progress. In phase II, the crack growth rate substantially increases in both directions, the crack length expands exponentially, and the propagation rate in the radial direction surpasses that in the other direction. These features are consistent with the bolt fracture morphology derived from the fatigue test: a crescent in the fatigue source area and nearly a semicircle in the propagation area.

Fig. 22 reveals that augmenting the stress range accelerates the crack growth rate in both directions, causing the high-strength bolt to fail under a reduced number of loading cycles. This occurs because crack propagation is strongly related to the stress field intensity at the crack front. An increased load amplifies the stress at this point, supplying the necessary stress for rapid material separation; hence, the crack extends swiftly.

The aforementioned analysis indicates that a swiftly enlarges in phase II, which is more favorable for load eccentricity, subsequently raising the stress on the effective section and consequently diminishing the bolt fatigue life in this phase. Consequently, the following section concentrates on the evolution of a during the fatigue failure process.

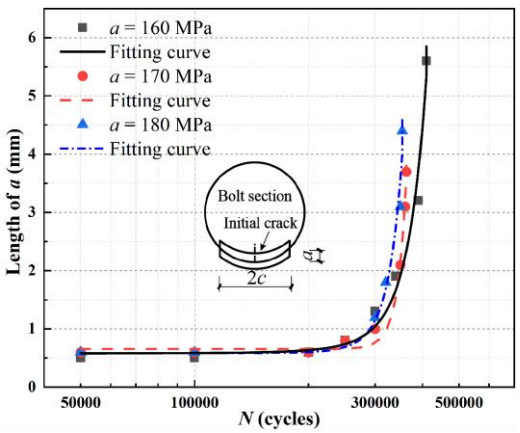

Fig. 23 The changes in a with loading cycles at different stress ranges

Fig. 23 demonstrates the changes in a in relation to the loading cycle number at various stress ranges: a starts to slowly grow with an increase in N. An elevated stress level quickens the fatigue damage accumulation rate, so a starts to rise at lower loading cycles: a $\Delta\sigma$ of 160, 170, and 180 MPa results in loading cycles of 3.00×10^5, 2.00×10^5, and 1.00×10^5, respectively. In the later stages of crack propagation, an increase in the stress range produces larger crack increments under the same number of loading cycles.

The equation for calculating the changes in a concerning N is derived from curve fitting. The correlation coefficients (R^2)) of the fitted curves all surpass 0.9, signifying that the fitted outcomes are optimal, as presented in Table 11.

Table 11
The fitted results of the a–N curves

$\Delta\sigma$ (MPa)	Fitted equation	Correlation coefficient (R^2)
160	$a = 8.322 \cdot 10^{-5} \cdot e^{N/47488.130} + 0.601$	0.979
170	$a = 1.909 \cdot 10^{-8} \cdot e^{N/19250.079} + 0.655$	0.989
180	$a = 2.426 \cdot 10^{-5} \cdot e^{N/29848.439} + 0.586$	0.970

Additionally, in fracture mechanics, the stress intensity factor is a crucial parameter governing the crack growth rate (da/dN). Therefore, we plot the variation of da/dN with ΔK_1 to characterize the fatigue crack propagation, as shown in Fig. 24.

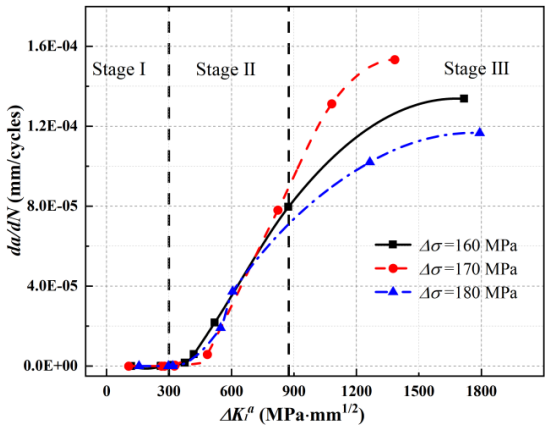

Fig. 24 The variation of da/dN with ΔK^a at various stress ranges

The curves can be divided into three stages based on the crack growth rate: stages I, II, and III. In stage I, da/dN is less than 10^{-10} mm/cycle, indicating that the crack does not grow in this stage. In stage II, da/dN typically ranges from 10^{-9} to 10^{-5} mm/cycle, a linear relationship exists between da/dN and ΔK_I, and a higher stress range corresponds to an increased crack propagation rate under the same ΔK_I. In stage III, da/dN is greater than 10^{-5} mm/cycle, and the crack size expands rapidly, leading to a swift fracture of the high-strength bolt. As a result, the contribution of stage III to the crack propagation life is generally disregarded. Fig. 24 indicates that stage III deviates from the commonly used da/dN–ΔK_I curve, which can be attributed to the fact that the standard da/dN–ΔK_I curve is derived from standard specimens with uniform thickness, whereas the bolts' thickness and surface shape change during crack propagation.

6. Conclusions

Axial-tensile constant-amplitude fatigue tests were carried out on M24 high-strength 20MnTiB steel bolts with a stress ratio of 0.3 in this study. The fatigue characteristics and failure mechanisms of the high-strength bolt was analyzed through regression analysis, strain analysis, and fracture surface analysis. Furthermore, the finite element method grounded in fracture mechanics was employed for examing the fatigue crack growth of the high-strength bolts, seeking to comprehend their fatigue crack propagation principles and elucidating the fracture mechanisms. The following conclusions were derived from the tests and numerical investigations:

- The S–N curve for the 20MnTiB steel high-strength bolt with an R value of 0.3 was established, revealing a threshold fatigue strength of 140.77 MPa at 2×10^6 loading cycles, which was 1.68 times greater than the fatigue life of the 35K steel bolt. This result demonstrated the superior fatigue performance of the former. Integrating a correction factor into the S–N curve was recommended to address the impact of material properties on the fatigue life of the bolt.
- Strain analysis indicated that the stable deformation stage constituted 87% of the high-strength bolt's fatigue life, and the strain variation of the specimen could be employed to roughly estimate the crack source location. The strain was reduced on the crack initiation side.
- A model for predicting the high-strength bolts' fatigue life was developed using XFEM and fracture mechanics, enabling the investigation of their fatigue crack propagation progression, albeit with a minor deviation.
- The law governing crack growth in the circumferential and radial directions was determined, and the fatigue crack growth mechanism of the bolt was clarified by simulating crack propagation. During the stable crack propagation stage, the crack primarily advanced along the bolt's circumferential direction, accounting for 85% of the crack propagation life, in accordance with the $\Delta\varepsilon$–n/N curve analysis results from the tests. In the unstable crack propagation stage, the crack length grew exponentially, and the radial growth rate exceeded the growth rate in the other direction. An increased stress range elevated the SIF at the crack front, promoting rapid crack expansion and consequently reducing the fatigue life of the high-strength bolt.

Acknowledgments

The research was financially supported by the National Natural Science Foundation of China [Grant No. 52278198] and the Fundamental Research Program in Shanxi Province, China [Grant No. 202203021211184].

References

[1] Mehmanparast, A., Lotfian, S. and Vipin, S.P., "A review of challenges and opportunities associated with bolted flange connections in the offshore wind industry", Metals, 10(6), 732, 2020.
[2] Weijtjens, W., Stang, A., Devriendt, C. and Schaumann, P., "Bolted ring flanges in offshore-wind support structures - in-situ validation of load-transfer behavior", Journal of Constructional Steel Research, 176, 106361, 2021.
[3] Yang, X., Lei, H.G. and Chen, Y.F., "Constant amplitude fatigue test research on M20 high-strength bolts in grid structure with bolt–sphere joints", Advances in Structural Engineering, 20(10), 1466-1475, 2016.
[4] Si Q, Ding Y, Zong L, and Liu H, "Mechanical properties and simulation method of structural steel after high cycle fatigue damage", Advanced steel construction, 19(1), 70-76, 2023.
[5] Yang, X. and Lei, H.G., "Constant amplitude fatigue test of high strength bolts in grid structures with bolt-sphere joints", Steel and Composite Structures, 25(5), 571-579, 2017.
[6] Qiu, B., Yang, X., Zhou, Z.C. and Lei, H.G., "Experimental study on fatigue performance of M30 high-strength bolts in bolted spherical joints of grid structures", Engineering structures, 205,110123, 2020.
[7] Jiao, J.F., Jia, P.P., Liu, Y., Liu, J.Q. and Lei, H.G., "Experimental study on constant amplitude fatigue of M24 high-strength bolts under critical stress ratio", Journal of Taiyuan University of Technology, 50(06), 749-755, 2019. (in Chinese)
[8] Jiao, J.F., L, Z.X., Guo, Q., Liu, Y. and Lei, H.G., "Constant-amplitude fatigue behavior of M24 high-strength bolt of end-plate flange connection", Structures, 34, 2041-2053, 2021.
[9] Liu, Y.Z., Chen, J., Zhang, X.F. and Tan, D., "Fatigue behavior of blind bolts under tensile cyclic loads", Journal of Constructional Steel Research, 148, 16-27, 2018.
[10] Tizani, W., Norashidah, Abd Rahman, N. and Pitrakkos, T., "Fatigue life of an anchored blind-bolt loaded in tension", Journal of Constructional Steel Research, 93, 1–8. 2014.
[11] Schaumann, P. and Rasmus, E., "Ermüdung sehr großer hv-schraubengarnituren", Stahlbau, 85(9), 604-611, 2016.
[12] Jiang, W.Q., Mo, Z., Yang, L.Q., Liu, J.L. and Niu, Z.B., "Theoretical study on early stage self-loosening of bolted joint in lattice transmission tower under transverse load", Advanced steel construction, 18(2), 574-584, 2022.
[13] Bartsch, H. and Feldmann, Markus., "Reassessment of fatigue detail categories of bolts and rods according to EC 3-1-9", Journal of Constructional Steel Research, 180, 106588, 2021.
[14] Li, Z.H., Han, K., Chen, T., Yang, H.S., Liu, P., and Lu, Y.H., "Fatigue life prediction of nuclear reactor main bolt based on temperature effect and size effect", International Journal of Fatigue, 152, 106443, 2021.
[15] Maljaars, J. and Euler, M., "Fatigue S–N curves of bolts and bolted connections for application in civil engineering structures", International Journal of Fatigue, 151, 106355, 2021.
[16] Lochan, S., Mehmanparast, A. and Wintle, J., "A review of fatigue performance of bolted connections in offshore wind turbines", Procedia Structural Integrity, 17, 276-283, 2019.
[17] Kaushik, V. and Anup, G., "Experimental and numerical investigation of mode-i & mode-ii fatigue crack growth in unidirectional composites using xiga-czm approach", International Journal of Fatigue, 134, 105461, 2020.
[18] Liu, H., Hu, D.Y., Wang, P.Q., Wang, X., Jin, S. A. and Gu, Y.X., "Experimental and numerical investigations on the influence of cold expansion on low cycle fatigue life of bolt holes in aeroengine superalloy disk at elevated temperature", International Journal of Fatigue, 132, 105390, 2020.
[19] Wang, Y.X., Ji, B.H., Fu, Z.Q. and Yao, Y., "Fatigue repairing craftmanship of deck-to-vertical stiffener weld in the steel bridge deck", Advanced steel construction, 15(3), 232-241, 2019.
[20] Fang L, Fu Z.Q., Ji B.H., and Kainuma S., "Propagation mode and characteristics of fatigue cracks in steel bridge deck after drilling ahead of the crack tip", Advanced steel construction, 18(2), 544-551, 2022.
[21] Gu M, Tong LW, Zhao XL, and Zhang YF., "Numerical analysis of fatigue behavior of welded cfchs t-joints", Advanced steel construction, 10(4), 476-497. 2015.
[22] Shi, J. X., Chopp, D., Lua, J., Sukumar, N. and Belytschko, T.," Abaqus implementation of extended finite element method using a level set representation for three-dimensional fatigue crack growth and life predictions", Engineering Fracture Mechanics, 77(14), 2840-2863, 2010.
[23] Malekan, M., Khosravi, A. and St-Pierre, L., "An Abaqus plug-in to simulate fatigue crack

growth", Engineering with Computers, 38(4), 2991-3005, 2021.
[24] Shu,Y.X., Li, Y.Z., Duan, M. and Yang,F., "An X-FEM approach for simulation of 3-D multiple fatigue cracks and application to double surface crack problems", International Journal of Mechanical Sciences, 130, 331-349, 2017.
[25] Samaei, M., Zehsaz, M. and Chakherlou, T. N., "Experimental and numerical study of fatigue crack growth of aluminum alloy 2024-T3 single lap simple bolted and hybrid (adhesive/bolted) joints", Engineering Failure Analysis, 59, 253-268, 2016.
[26] Bergara, A., Dorado J.I., Martín-Meizoso, A. and Martínez-Esnaola, J.M., "Fatigue crack propagation at aeronautic engine vane guides using the extended finite element method (XFEM)", Mechanics of Advanced Materials and Structures, 28(8), 861-873, 2021.
[27] Ngoula, D.T, Beier, H.T. and Vormwald, M., "Fatigue crack growth in cruciform welded joints: Influence of residual stresses and of the weld toe geometry", International Journal of Fatigue, 101, 253-262, 2017.
[28] Pandey, V.B., Singh, I.V., Mishra, B.K. Ahmad, S., Rao, A.V. and Kumar, V., "A new framework based on continuum damage mechanics and xfem for high cycle fatigue crack growth simulations", Engineering Fracture Mechanics, 206, 172-200, 2019.
[29] Lin, X.B, and Smith, R.A., "Finite element modeling of fatigue crack growth of surface cracked plates: Part III: stress intensity factor and fatigue crack growth life", Engineering Fracture Mechanics, 63(5), 541-556, 1999.
[30] Yang, F.P. and Kuang, P.J., "Fatigue crack growth for a surface crack in a round bar under multi-axial loading condition", Fatigue Fract. Eng. Mater. Struct, 28(11), 963-70, 2005.
[31] Kumar, S.S. and Prakash, R.V., " Effect of helix angle on the stress intensity factor of a cracked threaded bolt", Journal of Pressure Vessel Technology- Trans. ASME, 135(2), 12, 2013.
[32] Sharda, L, Mehmanparast, A. and Wintle, J., "A review of fatigue performance of bolted connections in offshore wind turbines" [A], The 3rd International Conference on Structural Integrity[C], Procedia Structural Integrity, 276-283, 2019.
[33] ISO 898-1: 2013, Mechanical properties of fasteners made of carbon steel and alloy steel — Part 1: Bolts, screws, and studs with specified property classes — Coarse thread and fine pitch thread. International Organization for Standardization, 2013.
[34] GB 50017-2017, Standard for design of steel structures. Ministry of Housing and Urban-Rural Development of the People's Republic of China, Beijing, People's Republic of China, 2017. (in Chinese)
[35] BS EN 1993-1-9:2005, Eurocode 3: Design of Steel Structures. Part 1-9: Fatigue, European Committee for Standardization; Brussels, Belgium, 2005.
[36] ANSI/AISC 360-16, Specification for Structural Steel Buildings, American Institute of Steel Construction, AISC Committee; Chicago, Illinois, USA, 2016.
[37] BS 7608:1993, Code of practice for fatigue design and assessment of steel structures, British Standards Institution; London, UK, 1993.
[38] Zhan, B., Liu, Y., Shang, W.N., Zhang, J.L. and Jiao J.F., "Experimental research on constant-amplitude fatigue characteristics of 8.8 grade M24 high-strength bolts", Ind Constr, 50(09), 122-127,2020. (in Chinese)
[39] Munn, B.S. and Li, K., Investigation into the effect of thread root condition on the high cycle fatigue performance of a metric threaded fastener [C]. ASME 2010 Pressure Vessels and Piping Division/K-PVP Conference. 2010.
[40] Fett, T., Stress intensity factors, t-stresses, weight functions [M]. Karlsruhe: Universit ätsverlag Karlsruhe, 2008.
[41] Paris, P. and Erdogan, F., "A critical analysis of crack propagation laws", Journal of Basic Engineering, 85 (4), 528-533, 1963.
[42] BS 7910:2013+A1:2015, Guide to methods for assessing the acceptability of flaws in metallic structures, British Standards Institution; London, UK, 2013.
[43] Hirt, M.A. and Fisher, J.W., "Fatigue crack growth in welded beams", Engineering Fracture Mechanics, 5(2), 415-429, 1973.
[44] Duan, H.C., "Numerical simulation and theoretical analysis of fatigue crack growth of steel pipe-welded hollow spherical joints", Ph.D. Dissertation, Taiyuan: Taiyuan University of Technology, 2019. (in Chinese)